Atmospheric
Measurement
Techniques
Discussions

Open Access

HelioFTH: combining cloud index principles and aggregated rating for cloud masking using infrared observations from geostationary satellites

B. Dürr[1], M. Schröder[2], R. Stöckli[3], and R. Posselt[3]

[1]Sunergy GmbH, Buchs SG, Switzerland
[2]Satellite Based Climate Monitoring, Deutscher Wetterdienst, Offenbach, Germany
[3]Federal Office of Meteorology and Climatology MeteoSwiss, Zurich, Switzerland

Correspondence to: B. Dürr (bruno.duerr@gmail.com)

Discussion Paper | Discussion Paper | Discussion Paper | Discussion Paper

AMTD

6, 1859–1898, 2013

Infrared-based cloud masking

B. Dürr et al.

Title Page

Abstract | Introduction

Conclusions | References

Tables | Figures

|◄ | ►|

◄ | ►

Back | Close

Full Screen / Esc

Printer-friendly Version

Interactive Discussion

Abstract

A cloud mask, cloud fractional coverage (CFC) and cloud top pressure (CTP) retrieval scheme called HelioFTH is presented. The algorithm relies on infrared (IR) window channel observations only. The scheme is applicable to the full temporal and spatial resolution of the Meteosat Visible and InfraRed Imager (MVIRI) and the Spinning Enhanced Visible and InfraRed Imager (SEVIRI) sensors. The main focus is laid on the separation of high cloud coverage (HCC) from low level clouds. CFC retrieval employs a IR-only cloud mask based on an aggregated rating scheme. CTP retrieval is based on a Heliosat-like cloud index for the MVIRI IR channel. CFC from HelioFTH, the International Satellite Cloud Climatology Project (ISCCP) DX and the Satellite Application Facility on Climate Monitoring (CM SAF) were validated with CFC from the Baseline Surface Radiation Network (BSRN) and the Alpine Surface Radiation Budget (ASRB) network. HelioFTH CFC differs by not more than 5–10 % from CM SAF CFC but it is higher than ISCCP-DX CFC. In particular the conditional probability to detect cloud-free pixels with HelioFTH is raised by about 35 % compared to ISCCP-DX. Also, the HelioFTH HCC was inter-compared to CM SAF and ISCCP-DX over different regions. The probability of false detection of cloud-free HCC pixels is 15 % lower for HelioFTH than for ISCCP-DX compared to the CM SAF HCC product over the full-disk area. HelioFTH could be used for generating a climate data record of cloud physical properties once its consistency and homogeneity is validated for the full Meteosat time series.

1 Introduction

Clouds play an essential role in determining the earth's radiation balance. They are essential factors regulating the global water cycle. Though of utmost relevance, the largest uncertainty of modeled climate predictions is related to the feedback of clouds to greenhouse gas changes (Trenberth et al., 2007). The automated identification of clouds in satellite measurements is a challenging task and a basic requirement for

processing of cloudy and clear sky products. The Global Energy and Water Cycle Experiment (GEWEX) Radiation Panel initiated the GEWEX Cloud Assessment Project in 2005 with the objective to determine the accuracy and uncertainty sources of cloud properties retrieved from satellite observations in order to ease usability for the climate
5 community. A summary of Cloud Assessment results is given in a GEWEX Newsletter in 2009 (available at: http://www.gewex.org). A well known and valuable cloud data set is the ISCCP DX data set (Rossow et al., 1996). It is the only global data set that is freely available, that covers more than 25 yr and that resolves the diurnal cycle.

The influence of the clouds on the surface incoming solar (SIS) radiation has been
10 quantified by different formulations of the satellite-based Heliosat cloud index (Cano et al., 1986; Beyer et al., 1996; Hammer et al., 2003; Dürr and Zelenka, 2009; Posselt et al., 2012). In this paper we propose an adaptation of the Heliosat cloud index principle to the atmospheric window IR channel at 10.8 µm of the Meteosat satellite to define a long-wave cloud index (LCI), which can be later used to deduce physical
15 cloud properties such as CTP and the surface downward long-wave (SDL) radiation based on the 2 m air temperature from surface measurements Dürr (2004) or numerical weather prediction (NWP) models. The detection of cloud-free pixels and the definition of the CFC is based on a modified formulation of the SPARC aggregated rating scheme (Khlopenkov and Trishchenko, 2007). The main requirements for the proposed scheme
20 are:

1. It shall be applicable to day-time and night-time MVIRI and SEVIRI observations without quality differences throughout the day. Therefore, the scheme can only be based on infrared window channel observations.

2. It shall be applicable to the full spatial and temporal resolution of MVIRI and SE-
25   VIRI observations.

3. No auxiliary input data from NWP models shall be necessary.

4. It needs to be able to separate low level from high level clouds. CFC can for instance be applied in the retrieval of free tropospheric humidity (FTH). FTH retrieval

Infrared-based cloud masking

B. Dürr et al.

is more reliable when restricted to either fully clear sky or low level cloud situations (Brogniez and Pierrehumbert, 2006).

The HelioFTH scheme is able to directly process satellite's raw IR sensor counts. The main advantage of processing raw counts is the possibility to formulate a self-calibrating LCI scheme designed for the processing of long-term IR time-series with several changes of satellite platforms, bit resolution of satellite counts and spatial resolution of the satellite pixels. This new method is thus applicable to the full METEOSAT time-series.

The most critical information for obtaining a realistic LCI is the apparent cloud-base temperature, which mainly determines the SDL radiation received at the surface. However, compared to visible radiation the path length of infrared radiation in clouds is short. Therefore it is not possible to retrieve the cloud-base temperature directly by Meteosat IR measurements. Thus a relation between the observed cloud-top temperature and the cloud-base temperature has to be formulated. Validation with surface measurements showed that in general the colder the cloud-top temperature, the larger the measured SDL at the surface, i.e. the warmer the cloud-base temperature. That means that the vertical extent of the clouds tends to increase, if the cloud-top reaches higher up in the troposphere. Therefore the following formulation for LCI is suggested:

$$LCI = 100 \left(1 - \frac{C - C_{min}}{C_{max} - C_{min}} \right), \tag{1}$$

with C being the instantaneous satellite's raw IR sensor count, while C_{max}, the maximum satellite's raw IR sensor count, corresponds to a cloud-free, clean and dry sky, and C_{min} corresponds to the coldest cloud-top temperatures.

The paper is structured as follows. Section 2 gives an overview of satellite and surface data used to obtain and validate the different HelioFTH cloud products. Section 3 describes the various processing steps of the HelioFTH scheme in detail. Section 4 contains the results of validation against independent surface cloud observations and

Full Screen / Esc

Printer-friendly Version

Interactive Discussion

the results of satellite inter-comparison with ISCCP-DX and CM SAF products. Section 5 concludes with a summary of the paper.

2 Data

CM SAF and ISCCP-DX cloud products are used to validate the MVIRI-based cloud
products. However most of the operational CM SAF cloud products (Schulz et al., 2008)
are processed since 2006 only, and Meteosat-7 was moved over the Indian Ocean in
summer 2006. Therefore the CM SAF team processed a off-line set of the CM SAF
cloud products based on SEVIRI data for April 2004, which is used as the reference
month for this paper.

2.1 Satellite data

The investigation area covers Meteosat full-disk which is roughly approximated by a
regular latitude/longitude grid from 60° S to 60° N and 60° W to 60° E in this paper.
Two regional areas were additionally analyzed: Europe (30° N–60° N, 40° W–40° E) and
Southern Africa (40° S–0° S, 10° W–30° E).

2.1.1 Meteosat-7

The MVIRI spatial resolution of IR channel 10.8 μm data (IR10.8) is 5 km × 5 km at
nadir and 2.5 km × 2.5 km for the visible (VIS) channel. Half-hourly (hereinafter referred
to as instantaneous) IR10.8 and VIS raw sensor counts from Meteosat-7 satellite for
April 2004 were obtained as level 1.5 OpenMTP files from EUMETSAT's U-MARF
archive.

2.1.2 ISCCP-DX

The 3-hourly ISCCP-DX product was obtained from the EOS data server (http://eosweb.larc.nasa.gov/PRODOCS/isccp/table_isccp.html) and the cloud flag was calculated according to Rossow et al. (1996, see Sect. 2.3.4). The ISCCP-DX cloud mask is based on a IR threshold test during night and a VIS (if available) or a near infrared threshold test (not available for Meteosat-7) during day.

2.1.3 CM SAF

An off-line set of hourly instantaneous CM SAF cloud products (Derrien and Gléau, 2005; Schulz et al., 2008; Reuter et al., 2009) based on SEVIRI data was processed for April 2004 and compared to HelioFTH and ISCCP-DX products.

2.2 Surface data

2.2.1 Longwave cloud index based on radiation data

For April 2004 surface radiation measurements were obtained from the ASRB network (Marty et al., 2002) as level 004 files. 2 m air temperature ($T_{2\,m}$) and relative humidity (RH) were measured by the Automatic network (ANETZ) and the Swiss Meteorological Network (SMN), respectively, both maintained by MeteoSwiss (Suter et al., 2006). Surface radiation data, air temperature and relative humidity from the BSRN were obtained from the BSRN FTP server at the Alfred Wegener institute (ftp://ftp.bsrn.awi.de). SIS and SDL radiation, $T_{2\,m}$ and RH were measured at all investigated surface sites. Partial Cloud Amount (PCA) in octa was estimated with the APCADA algorithm (Dürr and Philipona, 2004). A shortwave cloud flag (SCF) was used to detect high thin cirrus clouds during daytime (Dürr and Zelenka, 2009). Table 2 gives an overview of the subset of ASRB sites and BSRN stations, where the necessary input parameters were available for estimating cloud cover retrieved from surface observations.

Title Page

Abstract | Introduction

Conclusions | References

Tables | Figures

◄ | ►

◄ | ►

Back | Close

Full Screen / Esc

Printer-friendly Version

Interactive Discussion

Discussion Paper | Discussion Paper | Discussion Paper | Discussion Paper

The LCI observed at ASRB sites was first introduced by Dürr (2004) as the so-called cloud-free index saturation (CFI_{sat}). LCI observed at ASRB stations is defined as:

$$LCI = 100\frac{CFI - 1}{r}, \qquad (2)$$

with $r = CFI_{max} - CFI_{cloud-free}$, $CFI_{cloud-free} = \frac{\epsilon_{AC}}{\epsilon_{AC}} = 1$. The cloud-free index (CFI) is defined as:

$$CFI = \frac{\epsilon_A}{\epsilon_{AC}}, \qquad (3)$$

where $\epsilon_A = SDL/(\sigma T^4)$ is the apparent emissivity of the sky with T the absolute 2 m air temperature given in Kelvin, ϵ_{ac} is an empirical apparent emissivity of a cloud-free sky (Dürr and Philipona, 2004). A LCI value of 100 % indicates low clouds, where the longwave emission of the cloud is equal to the Plank emission of $T_{2\,m}$. LCI ≤ 0 % indicates cloud-free conditions, where SDL emitted by the sky is lower or equal the upper limit of SDL for cloud-free situations statistically obtained from site measurements.

All surface measurements were available as 10 min averages. In this paper the temporal resolution was reduced to 30 min intervals by using every third 10 min average only.

2.2.2 Synoptic cloud observations

Synoptic observations of total cloud amount (SYN) based on WMO-standards are available for all sites except Carpentras for different times as indicated in Table 2. Nighttime observations are available for Payerne only.

3 Formulation of the HelioFTH scheme

CFC, CTP and HCC are obtained from MVIRI raw IR sensor counts by use of the LCI based on the Heliosat cloud index principle and with a cloud-free flag c based on

a modified formulation of the SPARC scheme. Figure 1 shows the flow chart of the main processing steps of the HelioFTH scheme, which are described in detail in the following sections. The core element of the HelioFTH scheme is the cloud-free flag c, which separates cloud-free from cloudy pixels.

3.1 Definition of modeled maximum satellite count

LCI (Eq. 1) depends on a stable retrieval of C_{max} which is proportional to the maximum planetary brightness temperature. The diurnal cycle of C_{max} mainly depends on the solar geometrical parameters like day-length or the actual sun position. Mannstein et al. (1999) suggested a combination of cosine and sine functions to model the diurnal cycle of C_{max} over Northern Africa for each satellite pixel. However this function is not applicable for the short day-length over mid and higher latitudes during wintertime. Therefore the combination of cosine and sine functions was replaced by the bell-shaped curve in this paper:

$$C_{max} = a_0 + a_1(\exp(\frac{-2(\omega t - a_3)^2}{a_2^2}) +$$

$$0.1\sin(\omega t - a_3)), \tag{4}$$

where $\omega = 2\pi/N_{slot}$ (N_{slot} is the total number of Meteosat observation slots per day, e.g., $N_{slot} = 48$ for Meteosat-7), t denotes the slot number, a_0 is the minimum of the C_{max} diurnal cycle, a_1 is the amplitude of the bell-shaped curve, a_2 is the half-width of day-length in radians and a_3 is the true sun time at UTC=12 in radians. The half-width of the day-length a_2 is calculated by:

$$\delta = 23.45\frac{\pi}{180}\sin(\frac{2\pi}{365}(d_{yr} + 284)) \tag{5}$$

$$a_2 = \arccos(-\tan\phi\tan\delta) \tag{6}$$

where δ is the sun declination (radians), and ϕ latitude (radians), and d_{yr} the actual day of the year starting with 1 at the 1st of January. The true sun time a_3 is calculated by:

$$\theta = \frac{2\pi(d_{yr} - 1)}{365} \tag{7}$$

$$t_{eq} = 0.0172 + 0.4281\cos(\theta) - 7.3515\sin(\theta)$$
$$-3.3495\cos(2\theta) - 9.3619\sin(2\theta) \tag{8}$$

$$a_3 = (180 - \lambda + t_{eq}/4)\frac{\pi}{180}, \tag{9}$$

where t_{eq} is the equation of time, and λ is the longitude (degrees east). Parameters a_0 and a_1 in Eq. (4) have to be fitted to obtain the diurnal cycle of C_{max} for each satellite pixel (see Sect. 3.3).

3.2 Modification of SPARC scheme

Khlopenkov and Trishchenko (2007) published a scheme to detect cloud, snow and cloud shadows from AVHRR data called SPARC ("Separation of Pixels Using Aggregated Rating over Canada"). SPARC uses aggregated rating instead of branch rating within the cloud detection. The modified version of SPARC used in the HelioFTH algorithm employs the raw IR sensor counts (C) which are proportional to the planetary brigthness temperature. They are compared to a dynamic threshold $C_{max,real}$ which is proportional to the diurnal cycle of the surface skin temperature. In analogy to the T score suggested by SPARC, a temperature (T) score is calculated for the MVIRI IR counts:

$$T = (C - C_{max,real} - C_{offs})C_{scale}, \tag{10}$$

Title Page

Abstract | Introduction

Conclusions | References

Tables | Figures

|◄ | ►|

◄ | ►

Back | Close

Full Screen / Esc

Printer-friendly Version

Interactive Discussion

where $C_{\text{max,real}}$ is the realistic diurnal cycle of the maximum raw IR sensor count (see Sect. 3.4), C_{offs} is the offset and C_{scale} is the scale factor for C. C_{offs} and C_{scale} are obtained from a linear discriminant analysis (LDA[1]) by use of a training dataset:

Over land: Two low-land ASRB sites Locarno-Monti and Payerne were used from
5 October 2004–September 2005. A binary cloud-free (CFR) flag observed at surface radiation sites was defined as CFR = (PCA = 0 or SCF = 0), where PCA indicates the partial cloud amount from APCADA scheme and SCF a shortwave cloud flag from surface incoming shortwave radiation measurements (see also Sect. 2.2). This formulation of CFR allows the inclusion of cloud-free situations also during nighttime (PCA = 0),
10 and minimizes the occurrence of cirrus clouds during daytime (SCF = 0).

Over ocean: A Heliosat based processing scheme using a simplified formulation of SPARC was applied to MVIRI visible data to define a reference cloud mask over water since very few continuous radiation measurements are available over water. Clouds over water can easily be detected due to the large brightness contrast. Therefore, the
15 cloud mask based on visible data was used as a reference for cloud-free and cloudy pixels to determine the SPARC factors for HelioFTH over water.

The resulting C_{offs} factors over land ($-0.1314a_{0,\text{med}}$) and over water ($-0.0768a_{0,\text{med}}$) are dependent on the median value of a_0 over full-disk ($a_{0,\text{med}} = \text{median}(a_0)$), whereas C_{scale} over land (-0.0457) and over water (-0.0625) is a constant.
20 The spatial behavior of C is tested applying the SPARC uniformity score (U_{temp}) enhanced with the simultaneous testing of the temporal behavior of the C spatial differences. This allows to distinguish moving or developing clouds (indicated by enhanced changes of C) from the spatio-temporal evolution of cloud-free pixels. First the mean spatial difference of C to the 8 surrounding pixels is calculated for the current ($t0$) and
25 the 3 preceding slots ($t0 - 1, t0 - 2, t0 - 3$):

---

[1]LDA and the related Fisher's linear discriminant are methods used in statistics and machine learning to find a linear combination of features which characterize or separate two or more classes of objects or events. The resulting combination may be used as a linear classifier, or, more commonly, for dimensionality reduction before later classification.

Infrared-based cloud masking

B. Dürr et al.

$$\overline{\Delta C_t} = \sum_{i=-1,j=-1}^{i=1,j=1} \frac{(C_{t,i=0,j=0} - C_{t,i,j})}{8}, \tag{11}$$

where i and j indicate indices in column and row direction, respectively, and $t = t0, t0 - 1, t0 - 2, t0 - 3$. Afterwards the temporal variability C_{var} of $\overline{\Delta C_t}$ is calculated by summarizing the absolute differences of $\overline{\Delta C_t}$ between the adjacent slots normalized with the number of slot differences s involved:

$$C_{var} = \frac{\sum_{t=0}^{t=2} \left| \overline{\Delta C_{t0-t}} - \overline{\Delta C_{t0-t-1}} \right|}{s}. \tag{12}$$

Finally the spatio-temporal difference score D is calculated using LDA as follows:

$$D = (C_{var} - C_{var,offs})C_{var,scale}, \tag{13}$$

where $C_{var,offs}$ indicates the offset (over land: 0.9451, over water: 0.7043) and $C_{var,scale}$ the scale factor (over land: 0.4933, over water: 0.3304) of C_{var}.

The final expression for the aggregated rating F used in this paper is

$$F = T + D. \tag{14}$$

Values of F below zero indicate cloud-free, and above zero cloudy conditions. The stronger the deviation from zero, the more probable the classification becomes. However, the separation of cloud-free from cloudy pixels with aggregated rating based on a single channel only is not sufficient, yet. To refine the separation between cloud-free and cloudy pixels a cloud-free flag c based on the fuzzy-logic principle is introduced:

$$c = \begin{cases} 1 & \text{if } (F < F_{lim}) \\ F/F_{lim} & \text{if } (F \geq F_{lim}) \ \& \ (F \leq 0) \\ 0 & \text{if } (F > 0) | (F \text{ is undefined}) \end{cases}, \tag{15}$$

where $F_{lim} = -0.975$ is the maximum of the distribution of all F values from the training dataset for the ASRB sites Locarno-Monti and Payerne. The corresponding value for pixels over water is $F_{lim} = -0.775$. $c = 1$ means cloud-free, and $c = 0$ overcast and all values in between cloud-contaminated.

3.3 Daily update of C_{max}

To update C_{max} in Eq. (1) for each slot, the previous and instantaneous C values are weighted according to the cloud-free flag c:

$$C_{max} = cC_{max} + (1 - c)C. \tag{16}$$

Once a day the coefficients a_0 and a_1 of C_{max} are fitted if C_{max} was changed by Eq. (16) for at least one slot. All slots have equal weight for the fitting process, because C_{max} has already been weighted slot-wise by Eq. (16).

Limits for a_0 and a_1 are required to reduce the number of outliers of C_{max} due to misclassified clouds. These limits were obtained by eye inspection of a number of full-disk maps of C during summer- and wintertime. All thresholds are multiplied with a factor y defined as a function of sun declination δ and latitude ϕ to roughly mimic the yearly cycle of SIS:

$$y = \cos(\phi - \delta). \tag{17}$$

The minimum value of a_0 over water is $a_0 = 60 + 40y$ for $|\phi| < 70°$ and $a_0 = 20 + 80y$ for $|\phi| \geq 70°$. A lower ($a_1 = 10y$) and upper limit ($a_1 = 120y$) are applied for a_1 over land. In the current version of HelioFTH the limits are constant. The processing of longer time-series of MVIRI data covering Meteosat 2–7 may show that these limits have to be dynamic due to sensor gain changes, satellite changes and sensor degradation.

3.4 Realistic diurnal cycle of C_{max}

The main problem of using C_{max} in Eq. (1) is the fact that the ground measured diurnal cycle of C_{max} is often smaller due to the damping effect of clouds on SIS, where the

measured diurnal amplitude a_1 can be close to zero. Therefore for the final version of LCI C_{max} in Eq. (1) is replaced by $C_{max,real}$, which is defined here as:

$$C_{max,real} = a_0' + a_1'(\exp(\frac{-2(\omega t - a_3)^2}{a_2^2})$$

$$+0.1\sin(\omega t - a_3)) \qquad (18)$$

$$a_1' = a_1(1 - \frac{1}{100s}\sum_{t=1}^{t=s}(LCI_t')) \qquad (19)$$

$$a_0' = a_0 + \frac{a_1 - a_1'}{2}, \qquad (20)$$

where LCI_t' is calculated by Eq. (1), but using the previous value of $C_{max,real}$ for slot t. s is the number of available slots for that day. Here the range of LCI_t' is restricted to 0–100 % instead of the normal range of LCI values, which is restricted to −50–110 %.

3.5 Daily update of C_{min}

According to Eq. (1), determination of LCI requires the current minimum satellite's IR sensor count C_{min}, which is proportional to the coldest observed cloud top temperatures. For the retrieval of C_{min} the full-disk area is subdivided into 4 zonal bands: 90° S to 60° S, 60° S to 0° N, 0° N to 60° N and 60° N to 90° N. Once a day at 15:00 UTC, when the tropical thunderstorms in the center of the Meteosat viewing field reach their maximum height extension, the distribution of C for all cloud-contaminated or cloudy pixels (see Eq. 26) within a zonal band is calculated. The 10th percentile of this distribution gives the current $C_{min,t}$ value for each zonal band. A trailing 15 days window is then further used to determine the mean C_{min} value:

$$C_{min} = \frac{\sum_{t=1}^{15}C_{min,t}}{15}. \qquad (21)$$

1871

The resulting mean C_{min} value for each zone is finally interpolated to 1° latitudinal steps from 90° S to 90° N using a spline function. Thus C_{min} is constant for 1 day and the current formulation of C_{min} is only dependent on the latitude.

3.6 Correction of sudden satellite count changes

The application of raw sensor counts (C) causes problems if a satellite sensor changes, e.g., data of the backup satellite are used instead of the original counts. This may cause a sudden change of the median C value observed over the full-disk area. Coincidentally April 2004 was affected by such a sudden extreme change of the median value (C_{med} = median(C)) of C over the full-disk. Sudden extreme changes of C are monitored by:

$$C_{change} = \left| \frac{C_{med,t}}{C_{med,t-1}} - 1 \right|,\qquad(22)$$

with t indicating the current slot and $t-1$ the last available slot. C_{change} can notably affect a_0 and a_2, which are corrected immediately for slot t if necessary:

$$a_{i,t} = \begin{cases} a_{i,t-1} & \text{if } (C_{change} \leq 0.1) \\ \frac{C_{med,t}}{C_{med,t-1}} a_{i,t-1} & \text{if } (C_{change} > 0.1) \end{cases},\qquad(23)$$

with $i = 0$ or $i = 2$. Additionally the offset C_{offs} for the T test has to be updated by calculating the new median value of a_0 ($a_{0,med,t} = $ median(a_0, t)) and by multiplying with the corresponding factor over land or water. In the current formulation of the HelioFTH scheme daily constant factors are used. If a sudden extreme change occurs, the factors are changed immediately. Thus a couple of slots for that day will have unrealistic coefficients, which are not flagged in the current formulation of the HelioFTH scheme.

The sudden change on the 14 April 2004 at 09:00 UTC was caused by a change of the MVIRI calibration coefficients. The value of $\frac{C_{med,t}}{C_{med,t-1}}$ was 0.84, thus C_{med} dropped by approximately 16 %. This dramatically affects the retrieval of C_{max}, because most of

the pixels after the change of C would be misleadingly interpreted as overcast by the modified SPARC scheme (Sect. 3.2), and C_{max} would remain more or less unchanged after the sudden change. Some of these issues could be circumvented when calibrated radiances instead of sensor counts were used in the HelioFTH processing.

₅ ## 3.7 Definition of HelioFTH products

LCI contains implicit information about the cloud-top temperature and, thus, CTP. Based on empirical comparisons of HelioFTH LCI with ISCCP-DX and CM SAF CTP products we propose the following logarithmic relationship between CTP and LCI:

$$CTP = 10^{\left(3-\frac{LCI-LCI_{min}}{1.25(LCI_{max}-LCI_{min})}\right)}, \tag{24}$$

₁₀ where CTP is given in hectopascal (hPa) with $LCI_{max} = 100\,\%$, and $LCI_{min} = 0\,\%$. The minimum possible value of CTP is restricted to $10^{(3-110/125)} = 131.826\,hPa$, where the maximum possible value of LCI is 110 % (see Sect. 3.4). Thus the minimum value is steered by the factor 1.25 in the current formulation of Eq. (24). Only LCI values greater than LCI_{min} are used to calculate CTP. CTP is undefined for cloud-free pixels. The max-

₁₅ imum possible value of CTP follows the US standard atmosphere 1976 (COESA: US Commission/Stand Atmosphere (Compiler), Natl. Oceanic & Atmospheric Admin (Collaborator), Natl. Aeronautics & Space Admin (Collaborator), United States Air Force (Collaborator), 1976) and is defined as:

$$CTP_{max} = 1013.25\left(1-\frac{0.0065z}{288.15}\right)^{5.255}, \tag{25}$$

₂₀ where z is the mean pixel altitude in meters asl. CTP in Eq. (24) is set equal to CTP_{max} if $CTP > CTP_{max}$.

The HelioFTH cloud fractional coverage (CFC) product classes are based on the modified SPARC cloud-free flag c in Eq. (15):

$$CFC = \begin{cases} 1 & \text{if } (c \geq c_{lim}) \\ 2 & \text{if } (c > 0) \text{ \& } (c < c_{lim}) \\ 3 & \text{if } (c = 0) \\ 255 & \text{if } (c \text{ is undefined}) \end{cases}, \tag{26}$$

where CFC = 1 indicates cloud-free, CFC = 2 cloud-contaminated, CFC = 3 overcast and CFC = 255 undefined pixels. The limit $c_{lim} = 0.66$ was estimated by localizing the minimum position between the two peaks of cloud-free and cloud-contaminated values from the distribution of c at the ASRB sites Payerne and Locarno-Monti. ISCCP-DX and CM SAF CFC products are transformed to the same cloud classes using the corresponding ISCCP-DX and CM SAF products. However ISCCP-DX has no cloud-contaminated values, i.e. CFC = 2 is missing.

The HelioFTH high cloud coverage (HCC) product comprises all cloud-contaminated (CFC = 2) or overcast (CFC = 3) pixels, where $CTP \leq CTP_{lim}$. The threshold value CTP_{lim} is set to 700 hPa in the current version of HelioFTH, which corresponds to a cloud top height of about 3000 m a.s.l.

3.8 Verification approach

PCA values (cloud cover in octa, see Sect. 2.2) for surface radiation sites are transformed to CFC cloud classes in the following way:

$$CFC = \begin{cases} 1 & \text{if } (PCA \leq 1) \\ 2 & \text{if } (PCA > 2) \text{ \& } (PCA < 7) \\ 3 & \text{if } (PCA \geq 7) \\ 255 & \text{if } (PCA \text{ is undefined}) \end{cases}, \tag{27}$$

Title Page

Abstract | Introduction

Conclusions | References

Tables | Figures

I◄ | ►I

◄ | ►

Back | Close

Full Screen / Esc

Printer-friendly Version

Interactive Discussion

where CFC = 1 indicates cloud-free, CFC = 2 cloud-contaminated and CFC = 3 overcast. HCC flags for surface radiation measurements are missing for the time being, because the retrieval of high cloud coverage needs further investigations.

For validation purposes the CFC cloud classes 1–3 as defined in Eqs. (26 and 27) are linearly transformed to 0–1 to compare with the results published in Reuter et al. (2009):

$$CFC = \frac{(CFC - 1)}{2}, \tag{28}$$

where CFC = 0 indicates cloud-free, CFC = 0.5 broken clouds and CFC = 1 overcast conditions at the surface site.

For comparison of instantaneous CFC products from satellites with surface observations the nearest neighbor pixel values both in space and time were applied. Therefore the maximum time difference amounts to 5 min, and the maximum spatial difference roughly amounts to the half of the satellite product spatial resolution.

All satellite cloud products from HelioFTH, CM SAF and ISCCP-DX are provided on different grids. For inter-comparison purposes the HelioFTH and CM SAF products are reprojected to a regular latitude/longitude grid with 0.1° resolution, where the values at the grid points are selected with the nearest neighbor method. For comparison of HelioFTH and CM SAF with ISCCP-DX the grid resolution is reduced to 0.5° to account for the coarse spatial resolution of the ISCCP-DX products.

4 Results

In this section the validation results of the HelioFTH CFC with surface measurements from 3 ASRB and 3 BSRN sites are presented. Further, HelioFTH CTP, CFC and HCC is intercompared to the corresponding ISCCP-DX and CM SAF products. All presented results are based on one month of data from April 2004.

4.1 Validation

4.1.1 Validation of the CFC product

We used the definition of statistical quantities as defined in Appendix A suggested by Reuter et al. (2009, see Sect. 5), who compared CM SAF CFC with synoptic reports (SYN) for the year 2006. Their results (Table 2) are reproduced as the CM SAF–SYN results in this study.

The number of available PCA observations e.g. for daytime is 2–8 times higher than for SYN reports. Thus, due to the high temporal resolution during day- and nighttime PCA observations are an effective means for the statistical evaluation of satellite clouds retrievals. On the other hand, the low temporal resolution and also the lesser amount of available obseration of SYN especially during nighttime should always be kept in mind when evaluating the validation results.

The CM SAF–SYN results in Table 4 are in accordance to previous validation results by Reuter et al. (2009, see Table 2). Overall and site-specific HelioFTH–PCA and HelioFTH–SYN comparisons show consistent results with Kuiper Skill Score (KSS) values in the order of 0.7–0.9 except for Sede Boqer, whereas ISCCP-DX shows an average of 0.46 for the same quantity. Reuter et al. (2009) pointed out that false clear pixels are indicated if $P(\mathrm{cf_{rd}|cf_{sa}})$ is lower than $P(\mathrm{cf_{sa}|cf_{rd}})$ but false cloud pixels are indicated if $P(\mathrm{cc_{rd}|cc_{sa}})$ is lower than $P(\mathrm{cc_{sa}|cc_{rd}})$. Thus, HelioFTH detects more cloudy cases than the surface observations show (i.e., it is clear-sky conservative), especially for the semi-arid sites De-Aar and Sede Boqer, but not for the mountainous sites Davos and Jungfraujoch. At these two sites conditional probabilities of detecting cloudy situations by the satellite ($P(\mathrm{cc_{sa}|cc_{rd}})$) are in the order of 0.7 due to the misinterpretation of cloudy pixels as snowy surface in the current version of HelioFTH. These pixels are subsequently labeled as cloud free resulting in an underestimation of the cloudy conditions. This also leads to a negative CFC bias for Alpine sites. The low probability of detecting clouds in Sede-Boqer is the result of a misrepresented diurnal cycle as will be shown in Sect. 4.1.2. The average accuracy or fraction correct (FC) for HelioFTH is

lower than for CM SAF, but FC is increased in the order of 0.10 compared to ISCCP-DX. With the exception of the Alpine sites Davos and Jungfraujoch, HelioFTH CFC reveals a systematic positive bias in the order of 0.1–0.2, which is comparable to ISCCP-DX.

4.1.2 Validation of the diurnal cycle of the CFC product

The different CFC satellite products were separately validated with PCA and SYN observations in Table 5 for day, night and twilight conditions. Compared to PCA, HelioFTH shows the best performance during day (FC and KSS highest) and notably lower during night and twilight. Compared to SYN, night and twilight yield better agreement. HelioFTH detects more false cloud pixels during nighttime, i.e. the difference of $P(cc_{rd}|cc_{sa})$ to $P(cc_{sa}|cc_{rd})$ is larger. For HelioFTH–SYN, however, $P(cc_{sa}|cc_{rd})$ and $P(cc_{rd}|cc_{sa})$ are above 0.95, because nighttime SYN comparison is dominated by observations of the training site Payerne. The validation results of CM SAF data with PCA and SYN show an overestimation of cloudy cases during day (only SYN) and night (PCA and SYN) but an overestimation of clear cases during twilight (PCA and SYN). This features are again more pronounced in comparison with SYN. ISCCP-DX shows an extreme overestimation of cloudy cases and subsequently an extreme underestimation of clear cases during the whole day with a maximum at twilight. The KSS is, therefore, much lower than for HelioFTH and CM SAF. The FC, however, is only slightly lower because the high amount of false detections are not considered in FC as it is done in KSS.

Figure 2 shows the mean diurnal cycle for the ASRB sites Payerne, Davos and Jungfraujoch. ISCCP-DX cloudiness is overestimated at Payerne (top panel). CM SAF and SYN fit well, but there is a systematic positive bias of HelioFTH CFC when compared to SYN mainly during nighttime in Payerne. SYN observations contain a reasonable amount of thin, high clouds or clouds very close to the horizon which cannot be captured by the ASRB PCA but is apparently represented by CM SAF. The comparison for the high alpine sites Jungfraujoch and Davos in Fig. 2 (middle and bottom panel, respectively) indicates a systematic negative bias for HelioFTH. This behaviour

Infrared-based cloud masking

B. Dürr et al.

is connected to the misinterpretation of clouds as snow which was already mentioned in Sect. 4.1.1. CM SAF, on the other hand, shows a strong positive bias during daytime due to snow-cover misinterpreted as clouds as seen by the SEVIRI visible channels. The ISCCP-DX product indicates overcast conditions during the whole day, thus, it is very likely that the cold snow surface is misinterpreted as clouds in the ISCCP-DX IR cloud retrieval.

Figure 3 shows the mean diurnal cycles for the BSRN stations Carpentras (top), Sede-Boqer (middle) and De-Aar (bottom). At Carpentras (top), HelioFTH, CM SAF and ISCCP-DX show similar course of the diurnal cycle with CM SAF being at the lower end and Helio FTH at the upper end of ISCCP-DX. However, compared the BSRN measurements, all three satellite products overestimate CFC in the afternoon and evening. For the semi-arid site Sede-Boqer (Israel) the diurnal cycle in Fig. 3 (middle panel) is neither captured by CM SAF, ISCCP-DX nor by HelioFTH. CM SAF tends to underestimate cloudiness during the morning, whereas Helio FTH and ISCCP-DX overestimate CFC. This rises the question if these discrepancies are a problem of the surface measurements and the applied PCA algorithm or if the diurnal cycle is misrepresented in all three satellite products. The SYN report at 06:00 UTC reveals a large gap to the BSRN PCA value. The comparison for the De-Aar site (South Africa) in Fig. 3 (bottom) indicates a systematic positive bias for HelioFTH especially during the morning. It is likely that the diurnal course of $C_{\max}$ during night and morning is not well captured. ISCCP-DX again shows a strong positive bias during afternoon. CM SAF fits very well to the surface based CFC.

4.2 Intercomparison

4.2.1 Intercomparison of CTP, CFC and HCC products

The CTP, CFC and HCC products of the three different satellite datasets HelioFTH, CM SAF and ISCCP-DX are compared to each other. Tables 3, 6 and 7 show the results of

the CTP, CFC and HCC intercomparison for the three different satellite datasets over three different regions (see Sect. 2.1).

Table 3 shows the bias and median difference for the CTP product intercomparisons. On the full-disk the mean bias between the HelioFTH and CM SAF is 5 hPa and the median difference −45 hPa. The CTP differences for the EU and SA region have different signs. Thus, HelioFTH can have higher and lower cloud top heights compared to CM SAF depending on the region. The ISCCP-DX product shows systematically higher CTP values. Thus, ISCCP-DX cloud tops tend to be at a much lower altitude compared to HelioFTH and CM SAF.

In Table 6) $POFD_{cf}$ for the HelioFTH CFC product is 6 % lower than for ISCCP-DX both compared to CM SAF. FC for the CFC product is similar (81–84 %) for all three intercomparisons except for the comparison over the land surface only, where the amount of false CFC cloudy pixels indicated by the difference of $P(cc_{rd}|cc_{sa})$ and $P(cc_{sa}|cc_{rd})$ is considerably increased. The KSS is highest for the intercomparison between ISCCP-DX and CM SAF.

In Table 7 the probability of false detection of cloud-free pixels ($POFD_{cf}$) for the HelioFTH HCC product is 15 % lower than for ISCCP-DX both compared to CM SAF on full-disk. However there are large $POFD_{cf}$ differences between the different regions and over land, where HelioFTH HCC tends to overestimate cloudy pixels. The FC for the HCC product is in the order of 80–88 % for all three intercomparisons. The KSS is highest for the intercomparison between HelioFTH and ISCCP-DX.

Figure 4 shows HelioFTH CTP, CFC and HCC over the full-disk during daytime compared to the respective fields from CM SAF. The CTP anomaly map (top right) shows that HelioFTH produces higher CTP over the tropical regions (i.e., lower cloud tops) and gives lower CTP over the higher latitudes (i.e., higher cloud tops). The mismatch of HelioFTH CFC cloud-free pixels (middle right) compared to cloudy CM SAF pixels (light green pixels) is 8.8 % and mainly concentrated over the Atlantic, which is discussed in more detail in the next Sect. 4.2.2. Mismatches of HelioFTH CFC cloudy pixels and CM SAF cloud-free pixels (light purple pixels) are more pronounced over

land areas. The mismatches in HCC (lower right) occur mainly in the higher latitudes where the higher cloud tops (lower CTP) in HelioFTH lead to a positive cloud detection whereas CM SAF states clear sky because of the lower cloud tops (higher CTP) (light purple pixels). This happens in a total of 5.5 % of the pixels. The mismatch of clear

5　cases in HelioFTH and cloudy cases in CM SAF (light green pixels) occur in 11.9 % of all pixels. However, those mismatches do not occur in confined areas but are scattered all over the disc mainly over the Atlantic.

4.2.2　Intercomparison of the diurnal cycle of HCC over South Africa

HelioFTH, ISCCP-DX and CM SAF HCC were compared over South Africa for the

10　3 April on 03:00 UTC (nighttime) and 15:00 UTC (daytime).

During nighttime, the difference between HCC from HelioFTH and CM SAF (Fig. 5, top left) shows a cloudy-cloudfree mismatch (light purple pixels) over the stratocumulus area around 22° S/3° E and at the border of large cloudy areas. As stated above, those are most likely due to the higher cloud tops in HelioFTH. Mismatches of the other kind

15　(cloudfree-cloudy, light green pixels) are apparent closer to the Equator and are due to the higher cloud tops in CM SAF than in HelioFTH. The same latitudinal dependence of the mismatches are also found for the daytime differences (Fig. 5, bottom right).

Comparing HelioFTH HCC to ISCCP-DX HCC in Fig. 5 shows similar patterns for the cloudy-cloudfree mismatches (light purple pixels) for night- (middle left) and day-

20　time (middle right). However, the cloudfree-cloudy mismatches close to the Equator do not occur in the intercomparison with ISCCP-DX. This is due to the lower cloud top heigths in ISCCP-DX compared to HelioFTH. The last fact is supported by the comparison of HCC from ISCCP-DX with HCC from CM SAF (Fig. 5, bottom left and bottom right). Large areas closer to the Equator show a cloudfree-cloudy mismatch (light green

25　pixels) stating that ISCCP-DX does not have high clouds whereas CM SAF has.

The comparison of HCC between night- and daytime shows notable differences between HelioFTH/ISCCP-DX and CM SAF over the sea, which may be explained by including more spectral (day/nighttime) and visible (daytime) information from SEVIRI to

the CM SAF cloud retrieval algorithm. Therefore the simple IR-based HelioFTH products are probably less affected by discontinuities between land and open water, and between day- and nighttime compared to the CM SAF products.

5 Conclusions

For the first time the Heliosat method commonly used with visible channel data for cloud index calculations was applied to IR channel data for the detection of cloud physical properties. It uses Meteosat MVIRI raw IR channel counts and is self-calibrating. This strategy can account for instrument gain changes and sensor degradation until fully intercalibrated radiances become available (Goldberg et al., 2011). It provides a cloud mask, cloud fractional coverage (CFC), cloud top pressure (CTP) and a separation into high cloud coverage (HCC) and low level clouds on the full spatial and temporal METEOSAT resolution without requiring external boundary conditions from numerical weather prediction (NWP) models.

Cloud physical products from HelioFTH, ISCCP-DX and CM SAF were validated with ASRB and BSRN surface observations, and also intercompared over the full-disk, Europe and South Africa for April 2004. The performance of HelioFTH CFC validated with ASRB and BSRN surface measurements and synop observations is better than for ISCCP-DX CFC especially for the detection of cloud-free pixels. However, some of the clear sky pixels are false detections (e.g., detection of low clouds as snow) making HelioFTH a cloud conserving algorithm. CM SAF and ISCCP-DX, in contrast, are the result of clear-sky conservative algorithms because they detect actual clear-sky pixels as cloudy (e.g., detection of snow as cloud). The performance of HelioFTH CFC for the full-disk is only slightly improved as opposed to ISCCP-DX if intercompared with CM SAF CFC. These results for the detection of cloud-free pixels indicate some difficulties of the HelioFTH scheme to retrieve cloud-free pixels in areas for which its parameters were not trained, such as deserts, snow or open sea. The problems are more pronounced for the CFC than for the HCC product due to the presence of low

clouds near the surface. Thus, some differences between the modeled diurnal course of C_{max} and the diurnal course of the surface brightness temperature measured by the satellite are misinterpreted as low clouds in the current version of HelioFTH.

HelioFTH performs equally to the CM SAF cloud physical products. During daytime the use of the IR channel only has advantages over snow-covered areas where CM SAF misclassifies snow patches as clouds. However, HelioFTH has to deal with the opposite problem when misinterpreting clouds as snow. But this misinterpretation is not bound to a certain daytime so that day-night biases as in CM SAF are not occuring. Furthermore the CM SAF HCC product detects more clouds during daytime, when spectral information from the visible SEVIRI channels is applied. This effect is mostly pronounced over the sea. The probability of false detection of cloud-free HCC pixels compared to CM SAF is notably lower for the HelioFTH (19 %) than for ISCCP-DX (34 %), but only 10 % between HelioFTH and ISCCP-DX. Both HelioFTH and ISCCP-DX likely fail to detect thin cirrus clouds since they use a single IR channel only. The validation results further indicate that the daytime-nighttime CFC differences of CM SAF especially over snow and other bright surfaces need to be analyzed in more detail with regard to climate monitoring needs.

The results and conclusions are based on a preliminary analysis using only one month of data. Within the CM SAF framework HelioFTH will now be extended to alternatively also use visible channel data during daytime and to employ inter-calibrated radiances for Meteosat First and Second Generation. A continuous climate data record of cloud physical products will then have to be validated for consistency and homogeneity and intercompared for the full Meteosat record.

Appendix A

Statistical measures

The Kuiper skill score (KSS; (Hanssen and Kuipers, 1965)) determines the probability that a predicted event occurs, relative to its casual occurrence. Here, we apply it to satellite measurements (the predicted value; sat) and both to ground-based observations (the surface data) for surface validations or satellite measurements (the reference satellite data) for satellite inter-comparisons which are both referred to as reference dataset (rd) hereinafter. We use a contingency table (Table 1) that contains the number of observations derived from rd–sat being cloud-free–cloud-free, cloud-free–cloudy, cloudy–cloud-free, and cloudy–cloudy. Note that the contingency table for the surface validations contains only results from unambiguous synoptic observations that are 0, 1, 7, and 8 octa.

Using a, b, c, d from Table 1, various statistical measures are computed as follows:

- $\text{KSS} = \frac{ad - cb}{(a+b)(c+d)}$;

- Conditional probabilities:

  - $P(\text{cf}_{sa}|\text{cf}_{rd} = a/(a+b)$; the conditional probability of the satellite cloud detection classifying a scene as cloud free, given a cloud-free observation from the reference dataset,

  - $P(\text{cc}_{sa}|\text{cc}_{rd} = d/(c+d)$; the conditional probability of the satellite cloud detection classifying a scene as cloud covered, given a cloud-covered observation from the reference dataset,

  - $P(\text{cf}_{rd}|\text{cf}_{sa} = a/(a+c)$; the conditional probability of a cloud-free observation from the reference dataset, given a cloud-free satellite classification,

  - $P(\text{cc}_{rd}|\text{cc}_{sa} = d/(b+d)$; the conditional probability of a cloud-covered observation from the reference dataset, given a cloud-covered satellite classification,

- accuracy or fraction correct (FC; referred to as hit rate by (Reuter et al., 2009, see Sect. 5)): FC = $\frac{a+d}{a+b+c+d}$,

- probability of false detection of cloud-free pixels (POFD$_{cf}$): POFD$_{cf}$ = $c/(c+d)$.

References

Beyer, H. G., Costanzo, C., and Heinemann, D.: Modifications of the Heliosat procedure for irradiance estimates from satellite images, Sol. Energy, 56, 207–212, 1996. 1861

Brogniez, H. and Pierrehumbert, R. T.: Using microwave observations to assess large-scale control of free tropospheric water vapor in the mid-latitudes, Geophys. Res. Lett., 33, doi:10.1029/2006GL026240, 2006. 1862

Cano, D., Monget, J. M., Albuisson, M., Guillard, H., Regas, N., and Wald, L.: A method for the determination of the global solar radiation from meteorological satellite data, Sol. Energy, 37, 31–39, 1986. 1861

COESA: US Commission/Stand Atmosphere (Compiler), Natl. Oceanic & Atmospheric Admin (Collaborator), Natl. Aeronautics & Space Admin (Collaborator), United States Air Force (Collaborator): U.S. Standard Atmosphere, 1976 (NOAA Document S/T 76-1562), NOAA, NASA, USAF, 1st Edn., 1976. 1873

Derrien, M. and Gléau, H. L.: MSG/SEVIRI cloud mask and type from SAFNWC, Int. J. Remote Sens., 26, 4707–4732, 2005. 1864

Dürr, B.: The greenhouse effect in the Alps – by models and observations, Ph.D. thesis, Swiss Federal Institute of Technology Zurich, 2004. 1861, 1865

Dürr, B. and Philipona, R.: Automatic Cloud Amount Detection by Surface Longwave Downward Radiation Measurements, J. Geophys. Res., 109, 1–9, doi:10.1029/2003JD004182, 2004. 1864, 1865

Infrared-based cloud masking

B. Dürr et al.

Dürr, B. and Zelenka, A.: Deriving surface global irradiance over the Alpine region from ME-TEOSAT Second Generation data by supplementing the HELIOSAT method, Int. J. Remote Sens., 30, 5821–5841, doi:10.1080/01431160902744829, 2009. 1861, 1864

Goldberg, M., Ohring, G., Butler, J., Cao, C., Datla, R., Doelling, D., Gärtner, V., Hewison, T., Iacovazzi, B., Kim, D., Kurino, T., Lafeuille, J., Minnis, P., Renaut, D., Schmetz, J., Tobin, D., Wang, L., Weng, F., Wu, X., Yu, F., Zhang, P., and Zhu, T.: The Global Space-Based Inter-Calibration System, B. Am. Meteorol. Soc., 92, 467–475, doi:10.1175/2010BAMS2967.1, 2011. 1881

Hammer, A., Heinemann, D., Hoyer, C., Kuhlemann, R., Lorenz, E., Müller, R., and Beyer, H.: Solar energy assessment using remote sensing technologies, Remote Sens. Environ., 86, 423–432, 2003. 1861

Hanssen, A. and Kuipers, W.: On the Relationship Between the Frequency of Rain and Various Meteorological Parameters (with Reference to the Problem of Objective Forecasting), Vol. 81 of KNMI Meded. en verhand. (Reports and Essays), Staatsdrukkerij, 1965. 1883

Khlopenkov, K. V. and Trishchenko, A. P.: SPARC: New Cloud, Snow, and Cloud Shadow Detection Scheme for Historical 1-km AVHHR Data over Canada, J. Atmos. Ocean. Tech., 24, 322–343, doi:10.1175/JTECH1987.1, 2007. 1861, 1867

Mannstein, H., Broesamle, H., Schillings, C., and Trieb, F.: Using a meteosat cloud index to model the performance of solar thermal power stations, in: Eumetsat Conference, 239–246, Eumetsat, Copenhagen, Denmark, 1999. 1866

Marty, C., Philipona, R., Fröhlich, C., and Ohmura, A.: Altitude dependence of surface radiation fluxes and cloud forcing in the Alps: results from the alpine surface budget network, Theor. Appl. Clim., 72, 137–155, 2002. 1864

Posselt, R., Mueller, R., Stöckli, R., and Trentmann, J.: Remote sensing of solar surface radiation for climate monitoring – the CM-SAF retrieval in international comparison, Remote Sens. Environ., 118, 186–198, doi:10.1016/j.rse.2011.11.016, 2012. 1861

Reuter, M., Thomas, W., Albert, P., Lockhoff, M., Weber, R., Karlsson, K.-G., and Fischer, J.: The CM-SAF and FUB Cloud Detection Schemes for SEVIRI: Validation with Synoptic Data and Initial Comparison with MODIS and CALIPSO, J. Appl. Meteorol. Clim., 48, 301–316, doi:10.1175/2008JAMC1982.1, 2009. 1864, 1875, 1876, 1884

Rossow, W. B., Walker, A. W., Beuschel, D. E., and Roiter, M. D.: International Satellite Cloud Climatology Project (ISCCP): Documentation of new cloud Datasets, Tech. Rep. WMO/TD-No. 737, World climate research Programme (ICSU and WMO), Genf, 1996. 1861, 1864

Schulz, J., Albert, P., Behr, H.-D., Caprion, D., Deneke, H., Dewitte, S., Dürr, B., Fuchs, P., Gratzki, A., Hechler, P., Hollmann, R., Johnston, S., Karlsson, K.-G., Manninen, T., Müller, R., Reuter, M., Riihelä, A., Roebeling, R., Selbach, N., Tetzlaff, A., Thomas, W., Werscheck, M., Wolters, E., and Zelenka, A.: Operational climate monitoring from space: the EUMETSAT Satellite Application Facility on Climate Monitoring (CM-SAF), Atmos. Chem. Phys., 9, 1687–1709, doi:10.5194/acp-9-1687-2009, 2009. 1863, 1864

Suter, S., Konzelmann, T., Mühlhäuser, C., Begert, M., and Heimo, A.: SwissMetNet – the new automatic meteorological network of Switzerland: transition from old to new network, data management and first results, in: 4th International Conference on Experiences with Automatic Weather Stations (ICEAWS), Altis Park Hotel, Lisbon, 2006. 1864

Trenberth, K., Jones, P., Ambenje, P., Bojariu, R., Easterling, D., Tank, A. K., Parker, D., Rahimzadeh, F., Renwick, J., Rusticucci, M., Soden, B., and Zhai, P.: Observations: Surface and Atmospheric Climate Change, chap. Climate Change 2007: The Physical Science Basis. Contribution of Working Group I to the Fourth Assessment Report of the Intergovernmental Panel on Climate Change, edited by: Solomon, S., Qin, D., Manning, M., Chen, Z., Marquis, M., Averyt, K. B., Tignor, M., and Miller, H. L.: Cambridge University Press, Cambridge, United Kingdom and New York, NY, USA, 2007. 1860

Infrared-based cloud masking

B. Dürr et al.

Title Page

Abstract | Introduction

Conclusions | References

Tables | Figures

|◄ | ►|

◄ | ►

Back | Close

Full Screen / Esc

Printer-friendly Version

Interactive Discussion

Table 1. Contingency table of satellite and synoptic/reference satellite (reference dataset) observations.

		Satellite	
	Scenario	Cloud-free (cf)	Cloudy (cc)
Reference dataset	Cloud-free (cf)	a	b
	Cloudy (cc)	c	d

Table 2. Surface radiation sites for the development and the validation (except Locarno-Monti) of satellite cloud products over METEOSAT full-disk area.

Station	Abbr	Network	Altitude ASL	Latitude °N	°E	Location Longitude	Synop observation time UTC
Locarno-Monti	OTL	ASRB	370	46.1722	8.7875	South of the Alps	not used
Payerne	PAY	ASRB	490	46.8122	6.9423	Swiss plateau	0, 3, 6, 9, 12, 15, 18, 21
Davos	DAV	ASRB	1610	46.8130	9.8436	Swiss Alps	6, 12, 18
Jungfraujoch	JFJ	ASRB	3580	46.5474	7.9853	Swiss Alps	6, 9, 12, 15, 18
Carpentras	CAR	BSRN	100	44.0830	5.0590	South of France	NA
De Aar	DAA	BSRN	1287	−30.6667	23.9930	South Africa	6, 12, 18
Sede-Boqer	SBO	BSRN	500	30.9050	34.7820	Middle East	6, 18

Table 3. Bias = mean(satellite–satellite) and median = median (satellite–satellite) of CTP product inter-comparison given in hectopascal (hPa) for full-disk (FD), Europe (EU) and South Africa (SA) for April 2004. N indicates the number of compared values.

Region	HelioFTH minus CM SAF			ISCCP-DX minus CM SAF			HelioFTH minus ISCCP-DX		
	N	Bias	Median	N	Bias	Median	N	Bias	Median
FD	1.85×10^8	5	-45	7.35×10^6	108	45	7.67×10^6	-68	-85
EU	3.28×10^7	-56	-95	1.24×10^6	51	15	1.29×10^6	-89	-110
SA	2.08×10^7	47	-15	9.49×10^5	94	30	9.82×10^5	-29	-35

Discussion Paper | Discussion Paper | Discussion Paper | Discussion Paper | Discussion Paper |

AMTD

6, 1859–1898, 2013

Infrared-based cloud masking

B. Dürr et al.

Title Page

Abstract | Introduction

Conclusions | References

Tables | Figures

|◄ | ►|

◄ | ►

Back | Close

Full Screen / Esc

Printer-friendly Version

Interactive Discussion

Table 4. Average station-based results of HelioFTH (sa) and surface CFC observations (rd) for April 2004 (obs = reference cloud observation at the surface (PCA = partial cloud amount, SYN = synoptical observation), N = number of all available surface values, $N_{cf,cc}$ = number of only clear-cloudy surface values, FC = fraction correct, KSS = Kuiper Skill Score and bias = mean(satellite–surface)). For comparison the mean results for CM SAF and ISCCP-DX CFC products are also shown.

Site	Obs	N	$N_{cf,cc}$	$\overline{CFC}_{rd}$	$P(cf_{sa}\|cf_{rd})$	$P(cc_{sa}\|cc_{rd})$	$P(cf_{rd}\|cf_{sa})$	$P(cc_{rd}\|cc_{sa})$	FC	KSS	Bias
Mean	PCA	1360	752	0.46	0.81	0.90	0.90	0.76	0.84	0.71	0.10
CM SAF	PCA	658	435	0.48	0.87	0.90	0.88	0.86	0.91	0.77	0.02
ISCCP-DX	PCA	216	153	0.46	0.48	0.97	0.92	0.61	0.74	0.46	0.24
PAY	PCA	1397	837	0.53	0.72	1.00	0.99	0.84	0.88	0.72	0.20
DAV	PCA	1344	729	0.60	0.89	0.86	0.83	0.91	0.87	0.75	−0.06
JFJ	PCA	1386	811	0.62	0.99	0.71	0.71	0.99	0.83	0.70	−0.18
CAR	PCA	1401	857	0.41	0.75	1.00	1.00	0.74	0.86	0.75	0.22
DAA	PCA	1230	719	0.20	0.85	1.00	1.00	0.60	0.88	0.85	0.24
SBO	PCA	1401	562	0.37	0.68	0.81	0.90	0.50	0.72	0.49	0.17
Mean	SYN	136	74	0.57	0.95	0.92	0.85	0.92	0.92	0.87	−0.02
CM SAF	SYN	127	81	0.62	0.85	0.96	0.77	0.97	0.94	0.82	0.00
ISCCP-DX	SYN	134	89	0.57	0.42	0.99	0.88	0.73	0.84	0.41	0.20
PAY	SYN	226	125	0.61	0.86	1.00	1.00	0.95	0.96	0.86	0.12
DAV	SYN	89	42	0.66	1.00	0.93	0.87	1.00	0.95	0.93	−0.09
JFJ	SYN	147	94	0.77	1.00	0.74	0.52	1.00	0.80	0.74	−0.27
DAA	SYN	84	37	0.26	0.94	1.00	1.00	0.71	0.95	0.94	0.18

Table 5. Mean results of the comparison of different satellite (sa) products with surface (rd) CFC observations for all investigated sites for April 2004 [Prod = product origin, S = scenario (D = day, N = night, T = twilight), obs = reference cloud observation at the surface (PCA = partial cloud amount, SYN = synop observation), N = number of all available surface values, $N_{cf,cc}$ = number of only cloud-free or overcast surface values, FC = fraction correct, KSS = Kuiper Skill Score and bias = mean (satellite–surface)].

Prod	S	Obs	N	$N_{cf,cc}$	$\overline{CFC}_{su}$	$P(cf_{sa}|cf_{rd})$	$P(cc_{sa}|cc_{rd})$	$P(cf_{rd}|cf_{sa})$	$P(cc_{rd}|cc_{sa})$	FC	KSS	Bias
HelioFTH	D	PCA	695	369	0.47	0.86	0.94	0.94	0.85	0.90	0.81	0.08
HelioFTH	N	PCA	609	350	0.44	0.78	0.85	0.88	0.70	0.79	0.62	0.11
HelioFTH	T	PCA	55	34	0.47	0.73	0.84	0.87	0.67	0.78	0.57	0.11
CM SAF	D	PCA	306	176	0.54	0.80	0.95	0.92	0.96	0.96	0.75	0.02
CM SAF	N	PCA	317	231	0.44	0.86	0.86	0.89	0.78	0.87	0.72	0.02
CM SAF	T	PCA	36	27	0.49	0.96	0.78	0.79	0.90	0.88	0.74	−0.06
ISCCP-DX	D	PCA	115	76	0.46	0.50	0.97	0.92	0.63	0.76	0.47	0.24
ISCCP-DX	N	PCA	88	66	0.44	0.50	0.97	0.92	0.60	0.73	0.47	0.24
ISCCP-DX	T	PCA	22	16	0.58	0.44	1.00	1.00	0.75	0.80	0.44	0.26
HelioFTH	D	SYN	89	48	0.58	0.98	0.92	0.86	0.92	0.92	0.89	−0.02
HelioFTH	N	SYN	40	23	0.46	0.93	1.00	1.00	0.95	0.97	0.93	0.10
HelioFTH	T	SYN	22	12	0.75	1.00	0.93	0.75	1.00	0.94	0.93	−0.10
CM SAF	D	SYN	77	48	0.64	0.80	1.00	0.88	0.98	0.98	0.80	0.04
CM SAF	N	SYN	43	30	0.47	0.92	0.98	0.97	0.94	0.95	0.90	0.01
CM SAF	T	SYN	22	13	0.75	1.00	0.80	0.55	1.00	0.83	0.80	−0.20
ISCCP-DX	D	SYN	87	56	0.58	0.49	0.99	0.89	0.76	0.85	0.48	0.22
ISCCP-DX	N	SYN	54	38	0.36	0.70	0.95	0.91	0.50	0.80	0.66	0.09
ISCCP-DX	T	SYN	22	14	0.68	0.33	1.00	1.00	0.85	0.86	0.33	0.27

Table 6. Results of the satellite inter-comparison of cloud fractional coverage (CFC) for full-disk (FD), full-disk only over land (FDL), Europe (EU) and South Africa (SA) for April 2004. N indicates the number of compared values, FC = fraction correct and KSS = Kuiper Skill Score.

Region	N	$POFD_{cf}$	$P(cf_{sa}|cf_{rd})$	$P(cc_{sa}|cc_{rd})$	$P(cf_{rd}|cf_{sa})$	$P(cc_{rd}|cc_{sa})$	FC	KSS
CFC HelioFTH–CFC CM SAF								
FD	3.09×10^8	0.09	0.66	0.91	0.78	0.84	0.83	0.57
FDL	1.06×10^8	0.06	0.58	0.94	0.91	0.69	0.76	0.52
EU	5.29×10^7	0.08	0.72	0.92	0.79	0.88	0.86	0.64
SA	3.60×10^7	0.13	0.72	0.87	0.77	0.84	0.82	0.59
CFC HelioFTH–CFC ISCCP-DX								
FD	1.09×10^7	0.09	0.63	0.91	0.81	0.81	0.81	0.54
EU	1.83×10^6	0.09	0.64	0.91	0.79	0.83	0.82	0.56
SA	1.43×10^6	0.10	0.69	0.90	0.83	0.80	0.81	0.59
CFC ISCCP-DX–CFC CM SAF								
FD	1.06×10^7	0.15	0.79	0.85	0.74	0.88	0.83	0.64
EU	1.81×10^6	0.14	0.80	0.86	0.71	0.91	0.84	0.66
SA	1.41×10^6	0.17	0.84	0.83	0.74	0.90	0.83	0.66

Title Page

Abstract | Introduction

Conclusions | References

Tables | Figures

|◄ | ►|

◄ | ►

Back | Close

Full Screen / Esc

Printer-friendly Version

Interactive Discussion

Table 7. Results of the satellite inter-comparison of high cloud coverage (HCC) for full-disk (FD), full-disk only over land (FDL), Europe (EU) and South Africa (SA) for April 2004. N indicates the number of compared values, FC = fraction correct and KSS = Kuiper Skill Score.

Region	N	$POFD_{cf}$	$P(cf_{sa}|cf_{rd})$	$P(cc_{sa}|cc_{rd})$	$P(cf_{rd}|cf_{sa})$	$P(cc_{rd}|cc_{sa})$	FC	KSS
HCC HelioFTH–HCC CM SAF								
FD	3.09×10^8	0.19	0.83	0.81	0.84	0.80	0.82	0.64
FDL	1.06×10^8	0.11	0.82	0.89	0.90	0.79	0.85	0.70
EU	5.29×10^7	0.20	0.80	0.80	0.80	0.80	0.80	0.60
SA	3.60×10^7	0.34	0.89	0.66	0.82	0.79	0.81	0.56
HCC HelioFTH–HCC ISCCP-DX								
FD	1.09×10^7	0.10	0.81	0.90	0.94	0.73	0.85	0.72
EU	1.83×10^6	0.09	0.76	0.91	0.93	0.70	0.81	0.66
SA	1.43×10^6	0.11	0.87	0.89	0.96	0.69	0.88	0.76
HCC ISCCP-DX–HCC CM SAF								
FD	1.06×10^7	0.34	0.93	0.66	0.74	0.90	0.80	0.59
EU	1.81×10^6	0.32	0.91	0.68	0.75	0.88	0.80	0.60
SA	1.41×10^6	0.42	0.96	0.58	0.79	0.89	0.82	0.54

Fig. 1. Flow chart of HelioFTH processing scheme.

Infrared-based cloud masking

B. Dürr et al.
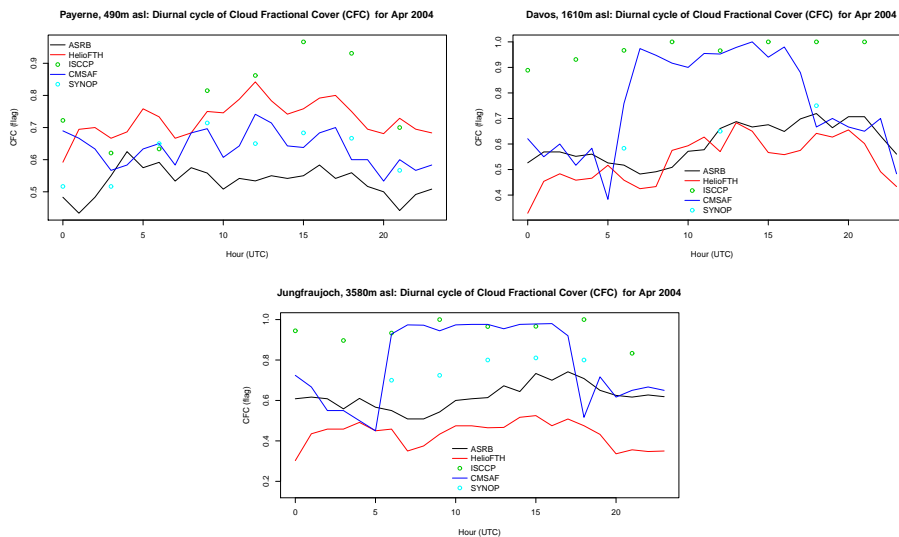
Fig. 2. Mean diurnal cycle of CFC for ASRB sites for April 2004.
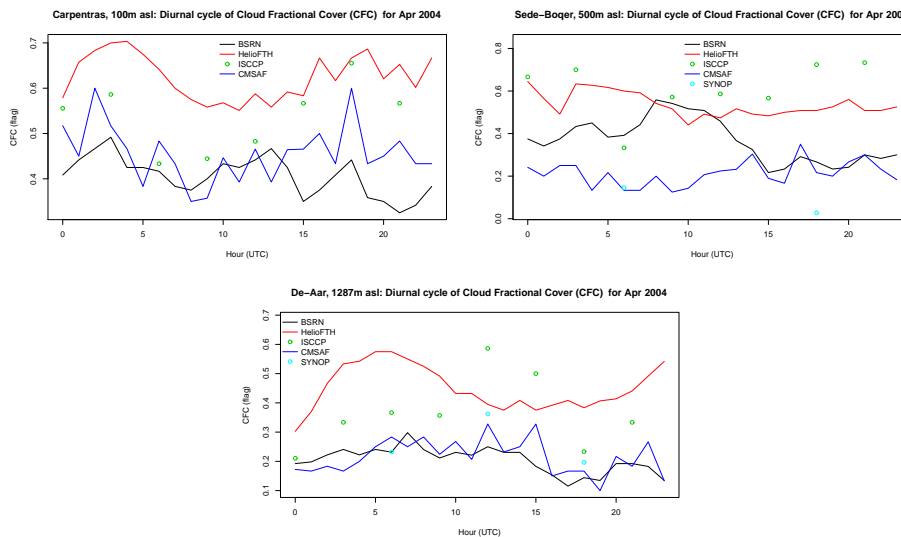
Fig. 3. Mean diurnal cycle of CFC for BSRN sites for April 2004.
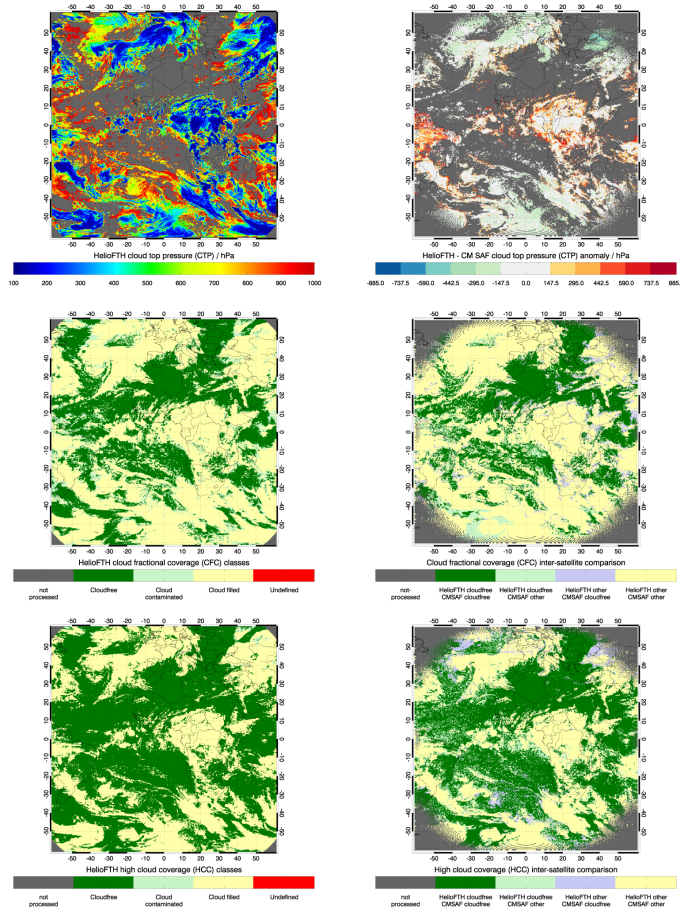
Fig. 4. 3 April 2004, 15:00 UTC: cloud top pressure (CTP), cloud fractional coverage (CFC) and high cloud coverage (HCC) for HelioFTH (left hand side). Categorical differences of HelioFTH products to CM SAF CTP, CFC and HCC (right hand side) over the full-disk area.

Title Page

Abstract | Introduction

Conclusions | References

Tables | Figures

◀ | ▶|

◀ | ▶

Back | Close

Full Screen / Esc

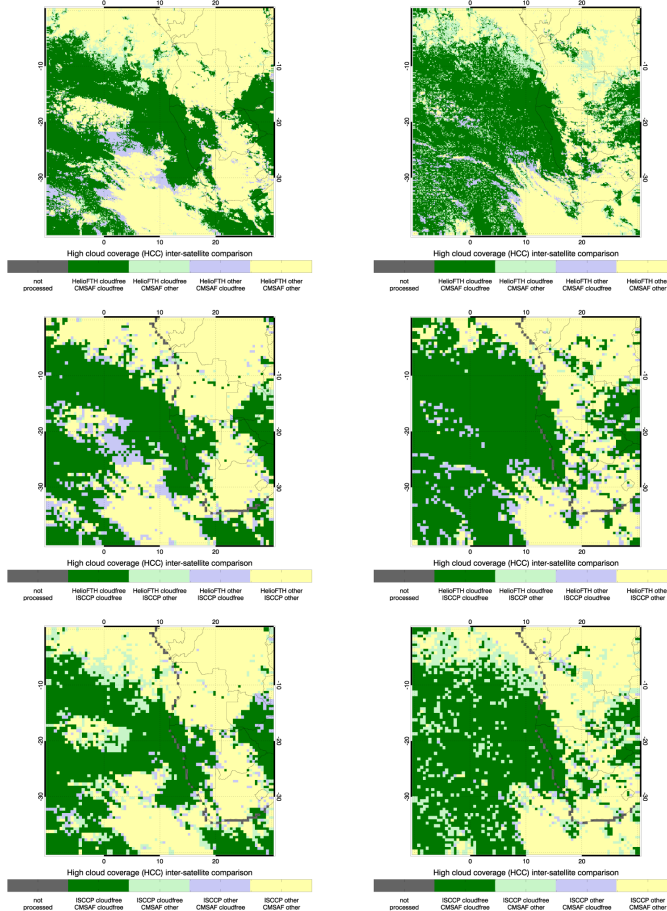Printer-friendly Version

Interactive Discussion

Fig. 5. 3 April 2004: categorical differences in high cloud coverage (HCC) for HelioFTH–CM SAF (top row), HelioFTH–ISCCP-DX (middle row) and ISCCP-DX–CM SAF (bottom row) for nighttime at 03:00 UTC (left column) and daytime at 15:00 UTC (right column).